ACS APPLIED MATERIALS & INTERFACES

Research Article

www.acsami.org

$CaMg_2Al_{16}O_{27}:Mn^{4+}$-based Red Phosphor: A Potential Color Converter for High-Powered Warm W-LED

Bo Wang,[†] Hang Lin,*[,†,‡] Ju Xu,[†,‡] Hui Chen,[†] and Yuansheng Wang*[,†,‡]

[†]Key Laboratory of Design and Assembly of Functional Nanostructures, Fujian Institute of Research on the Structure of Matter, Chinese Academy of Sciences, University of Chinese Academy of Sciences, Fuzhou, Fujian 350002, People's Republic of China

[‡]Fujian Provincial Key Laboratory of Nanomaterials, Fujian Institute of Research on the Structure of Matter, Chinese Academy of Sciences, Fuzhou, Fujian 350002, People's Republic of China

Supporting Information

ABSTRACT: New non-rare-earth-based oxide red phosphor discovery is of great interest in the field of energy-efficient LED lighting. In this work, a novel blue-light activated $CaMg_2Al_{16}O_{27}:Mn^{4+}$ (CMA:Mn^{4+}) phosphor, showing strong red emission peaked at ~655 nm under 468 nm excitation, is prepared by a solid-state reaction route. The microstructure and luminescent performance of this red-emitting phosphor are investigated in detail with the aids of X-ray diffraction refinement, diffuse reflection spectra, steady-state photoluminescence spectra and temperature-dependent PL/decay measurements. The crystal field strength (Dq) and the Racah parameters (*B* and *C*) are carefully calculated to evaluate the nephelauxetic effect of Mn^{4+} suffering from the CMA host. After incorporating CMA:Mn^{4+} and YAG:Ce^{3+} phosphor microcrystals into the glass host via a "phosphor-in-glass (PiG)" approach, warm white-light is achieved in the assembled high-powered w-LED device, thanks to the improved correlated color temperature and color rendering index.

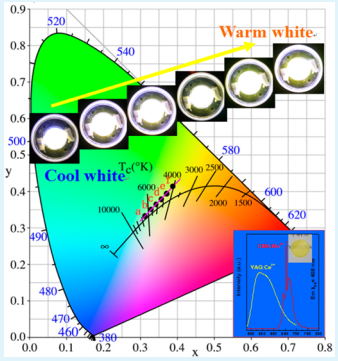

KEYWORDS: *phosphor in glass, Mn^{4+}, luminescent property, red phosphors, aluminates*

1. INTRODUCTION

White light-emitting diodes (w-LED), as promising candidates to replace conventional incandescent and fluorescent lamps, have received increasing attention in recent years due to their admirable merits of high luminous efficiency, low energy cost and robustness.[1−6] The current leading commercial w-LED technology is based on a "blue chip + yellow phosphor" strategy, i.e., the yellow phosphor converter YAG:Ce^{3+} dispersed in epoxy or silicone is directly packed on the blue InGaN chip. When driven by a certain current, the emitted yellow light from YAG:Ce^{3+} pluses the transmitted blue light, jointly constituting white luminescence. However, in practical application such design suffers some technical weaknesses. One big problem is the innate deficiency in red components, which leads to high correlated color temperature (CCT) and low color rendering index (CRI) for the white light.[7,8] The other one is the notorious poor thermal stability and weak thermal conductivity of the organic binders, which result in luminous decay and color-shift of the phosphors under long-term heat radiation.[9,10] To circumvent the above drawbacks, an additive red phosphor with ideal luminescent performance is highly demanded; besides, developing optimal inorganic encapsulating materials for accommodating the phosphors is of vital importance.

Among the state-of-the-art red phosphors, the Eu^{2+}, Ce^{3+} doped nitrides (such as $CaAlSiN_3:Eu^{2+}$ and $M_2Si_5N_8:Ce^{3+}$ (M = Ca, Sr, Ba)) are most commercialized;[11,12] however, their weaknesses are also obvious, mainly due to the critical synthetic requirements (typically prepared under 1800 °C, 0.5 MPa N_2 pressure) and serious photon reabsorption phenomenon (the photons emitted from the yellow or green phosphor can be absorbed by the red one, causing color change and luminous reduction).[13] As an alternative, the non-rare-earth Mn^{4+} doped red phosphors offer important advantages in these respects and thus have gained increased attention recently.[14−16] Mn^{4+} is featured by the $3d^3$ electron configuration with electrons located in an outer orbit, which causes its optical property heavily affected by the matrix; in the other words, the red emitting wavelengths of spin-forbidden Mn^{4+}: $^2E_g \rightarrow {}^4A_{2g}$, consisting of R line and the associated vibronic sidebands, are highly dependent on the covalency of the "Mn^{4+}-ligand" bonding.[17,18] Fluoride compounds are appropriate hosts for Mn^{4+}, in which Mn^{4+} exhibits the most intense excitation band locating at ~460 nm and very sharp red emission lines peaking at ~630 nm.[18] However, its sustainability under moisture environment seems to be a problem and should be further examined; moreover, in the synthesizing process, the required toxic HF solution is very harmful to environment.[19] In contrast, oxide compounds show much high chemical stability with an eco-friendly preparation procedure. Up to date, the Mn^{4+} doped oxides, including $CaAl_4O_7$, $Sr_4Al_{14}O_{25}$, $CaAl_{12}O_{19}$, $CaZrO_3$, $LaAlO_3$ and so on, have been extensively investigated,

Received: October 22, 2014
Accepted: November 27, 2014
Published: November 27, 2014

showing promising capabilities as good red converters for w-LED.[20−22]

As known, only Mn^{4+} in octahedral crystal field can emit red light;[15,16,18] therefore, searching for a host providing abundant octahedral sites for Mn^{4+} would be critical to achieving efficient red emissions. This inspires us to synthesize $CaMg_2Al_{16}O_{27}$ (CMA) compound, which belongs to a magnetoplumbite-related family, has never been studied as a luminescent host before, to our best knowledge. As displayed in Figure 1, the

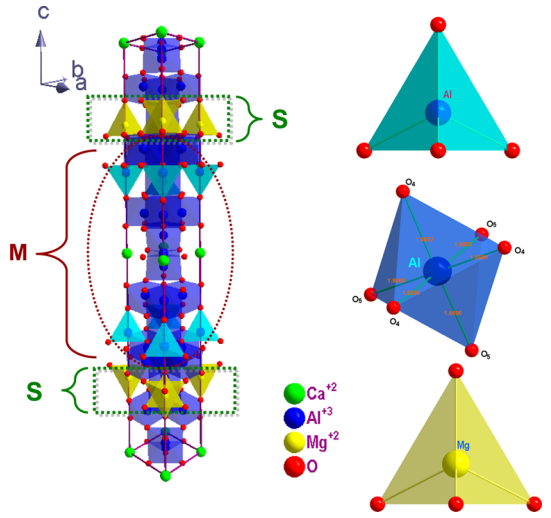

Figure 1. Schematic illustration of crystal structure in CMA, showing the stacking sequence of $(MS)_n$, and the coordination environment of the $[AlO_4]$ tetrahedron, $[AlO_6]$ octahedron and $[MgO_4]$ tetrahedron.

crystal unit cell of CMA is composed of two types of structural units, i.e., M ($CaAl_{12}O_{19}$, magnetoplumbite unit) and S ($Mg_2Al_4O_8$, spinel unit), stacking in a sequence of $(MS)_n$.[23−25] In such a big unit cell, there are huge amounts of the $[AlO_6]$ octahedral coordinated sites, offering great capacity to accept Mn^{4+} substitutes. It is also found that the Mn^{4+}-preferred $[AlO_6]$ layer is regularly separated by the Mn^{4+}-unoccupied $[AlO_4]$ or $[MgO_4]$ layer in the direction along the *c*-axis. Such a layered-structure is favorable to isolate Mn^{4+} ions from the local perturbations, thereby hopefully enabling the high efficiency of luminescence, as pointed out by Peng et al.[16]

To overcome the adverse effect of applying organic material as the encapsulant in w-LED, the lately developed phosphor-in-glass (PiG) technique has been proved to be a good solution. PiG is a composite of phosphors and several carefully selected glass components fabricated via a viscous sintering process at an optimal temperature (<1000 °C). During sintering, the glass components are totally melted while the phosphors remain solid and distribute uniformly in the glass matrix as much as possible.[26−29] It is expected that the excellent luminescent performance deriving from phosphors can be retained, and the inorganic glass matrix affords advantageous thermal/chemical stability. Previously, our group has innovatively reported the fabrication of $YAG:Ce^{3+}$ PiG color converter for w-LEDs, which exhibits a luminous efficacy (LE) of 124 lm/W, a correlated color temperature (CCT) of 6674 K and a color rendering index (CRI) of 70.[30] Herein, the synthesized $CMA:Mn^{4+}$ red phosphors were successfully introduced into the $YAG:Ce^{3+}$ PiG composite to tune the CCT and CRI, aiming to achieve high-powered warm w-LED lighting sources.

2. EXPERIMENTAL SECTION

2.1. Sample Preparation. A series of $CaMg_2Al_{16-x}O_{27}:xMn^{4+}$ (x = 0.016, 0.032, 0.08, 0.16, 0.24 and 0.48) powder samples were synthesized by the conventional high-temperature solid-state reactions. The starting materials of $CaCO_3$ (99.9%), MgO (99.9%), Al_2O_3 (99.9%) and $MnCO_3$ (99.9%) were weighted according to the stoichiometric ratio. 3.5 wt % H_3BO_3 (99.9%) was used as a flux. The mixed powders were ground in an agate mortar for 40 min, prefired at 800 °C for 1 h and subsequently sintered at 1550 °C for 6 h in the air.

To achieve the luminescent PiG, previously reported precursor glass with composition of 10-30 B_2O_3, 10-30 Sb_2O_3, 5-30 TeO_2, 10-25 ZnO, 5-20 Na_2O, 0-10 La_2O_3, 0-10 BaO were first fabricated via the conventional melting−quenching route.[30] Then, the obtained glass were crushed and milled into powders and mixed well with the phosphors of $CMA:Mn^{4+}$ and commercial $YAG:Ce^{3+}$ by using a ball grinder. The mixing weight ratio (%) of precursor glass powder: $CMA:Mn^{4+}:YAG:Ce^{3+}$ was 95 − y:y:5 (y = 1, 3, 5, 7 and 9, respectively). The mixture was sintered in a platinum crucible at 570 °C for 20 min with stirring. Subsequently, the melt was poured into a preheated copper mold to form the PiG composite, which was further annealed at 260 °C for 5 h to relinquish inner stress, cut into the desired dimensions (φ 12 mm disks with thickness of 0.4 mm) and polished for optical characterization.

2.2. Characterizations. Phase identification of all the as-obtained samples were carried out by using a powder diffractometer (Rigaku, Ultma IV), operating at 3 kW. The continuous scanning rate for phase determination was 5°/min, while the scanning rate for Rietveld analysis was 8 s per step with a step size of 0.02°. The microstructures of $CMA:Mn^{4+}$ powders and PiG were studied using a scanning electron microscopy (SEM, JSM-6700F) instrument equipped with an energy-dispersive X-ray spectroscopy (EDS) system. The diffuse refection spectra (DRS) of powder samples were measured by an UV−vis-NIR spectrophotometer (PerkinElmer, Lambda 900), using $BaSO_4$ as a standard reference. The photoluminescence (PL), photoluminescence excitation (PLE), temperature-dependent PL spectra and decay curves were recorded by a spectrophotometer (Edinburgh Instruments, FLS920) equipped with both continuous (450 W) and pulsed xenon lamps as the light source. The quantum efficiency (QE) measurements were performed using a barium sulfate coated integrating sphere that attached to the spectrophotometer. The internal QE (η_{int}), defined as the ratio of the number of photons emitted (I_{em}) to the number of photons absorbed (I_{abs}), is expressed as

$$\eta_{int} = \frac{I_{em}}{I_{abs}} = \frac{\int L_S}{\int E_R - \int E_S} \quad (1)$$

where L_S is the emission spectrum of the sample, E_S and E_R are the spectra of excitation light with and without the sample in the integrating sphere. The external QE (η_{ext}) is expressed as $\eta_{ext} = \eta_{int} \times \varepsilon_{abs}$, where ε_{abs} represents absorption efficiency of the sample. The values for LE, CCT, CRI and chromaticity coordinate of the PiG-based w-LED were measured in an integrating sphere of 50 cm diameter, which was connected to a CCD detector with an optical fiber (HAAS-2000, Everfine Photo-E-Info Co. Ltd.).

3. RESULTS AND DISCUSSION

3.1. Crystal Structure Analysis of $CMA:Mn^{4+}$. Figure 2a exemplarily shows the XRD pattern of $CMA:0.08Mn^{4+}$ along with the corresponding Rietveld structure refinement conducted by a general structure analysis system (GSAS) program. The refinement was proceeded by adopting the crystallographic data of $CaMg_2Al_{16}O_{27}$ (ICSD #81081) as an initial model and converges to R_{wp} = 8.9%, R_p = 7.3% and χ^2 = 2.86%, which indicates the refined atom position, fraction factors and temperature factors of the sample well satisfy the reflection conditions.[31] The final refined results confirm the single phase nature of the $CaMg_2Al_{16}O_{27}$ that is crystallized in a hexagonal *P*6mc space group with lattice parameters of $a = b$ = 5.603 Å, c

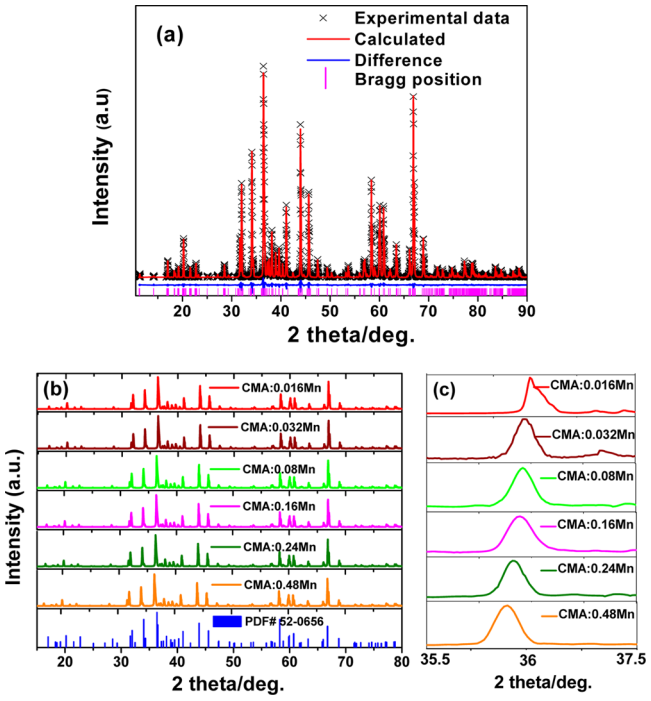

Figure 2. (a) Experimental XRD data, the corresponding Rietveld refine results, the Bragg reflections and the profile difference between experimental and calculated values of CMA:0.08Mn^{4+} sample; (b) XRD patterns of CMA:$x$$Mn^{4+}$ (x = 0.016−0.48), and the standard data of CMA phase (PDF #52-0656) as a reference; (c) magnified XRD curves in the range of 35.5−37.5°.

= 31.355 Å. The calculated unit cell volume (V = 851.66 $Å^3$) is slightly larger than that (V = 851.5 $Å^3$) of pure CMA crystal, probably caused by the preferable substitution of Mn^{4+} for Al^{3+} in octahedral sites, because the effective ionic radii (r) of Mn^{4+} (r = 0.535 nm, CN = 6) is larger than that of Al^{3+} (r = 0.530 nm, CN = 6).[32] Figure 2b displays the XRD patterns of CMA:$x$$Mn^{4+}$ (x = 0.016, 0.032, 0.08, 0.16, 0.24 and 0.48). All the diffraction peaks in these samples can be exactly assigned to the pure $CaMg_2Al_{16}O_{27}$ (PDF #52-0656), indicating Mn^{4+} doping does not influence the crystal structure significantly. With the increase of Mn^{4+} concentration, the peaks show a gradual shift toward the smaller 2θ angels compared to that of pure CMA, ascribing to that more Mn^{4+} occupy Al^{3+} sites. To achieve the charge balance, Mn^{4+} may form pairs by trapping an interstitial O^{2-} ions and replace a couple of neighboring Al^{3+} ions.[33]

3.2. Luminescence Properties of CMA:Mn^{4+} Phosphors. The diffuse reflection (DR) spectra of CMA doping with various Mn^{4+} contents are shown in Figure 3. One can see two typical strong spin-allowed Mn^{4+}: $^4A_{2g} \rightarrow {}^4T_{1g}$ and Mn^{4+}: $^4A_{2g} \rightarrow {}^4T_{2g}$ transitions peaking at ~345 nm (28 985 cm^{-1}) and ~468 nm (21 367 cm^{-1}) and a weak distinguishable spin-forbidden Mn^{4+}: $^4A_{2g} \rightarrow {}^2T_{2g}$ one locating at ~390 nm (25 641 cm^{-1}), which are similar to the experimental results reported previously.[34] As will be discussed hereafter, the broad band at ~345 nm, falling in the bandgap of CMA host, is composed of the Mn^{4+}: $^4A_{2g} \rightarrow {}^4T_{1g}$ and the Mn^{4+}−O^{2-} charge transfer (CT) transitions, because it exhibits slight red shift with increasing of Mn^{4+} concentration.

Figure 4 demonstrates the typical PLE and PL spectra of CMA:0.08Mn^{4+}. The PLE spectrum monitored at 655 nm shows several excitation bands ranging from 250 to 550 nm that

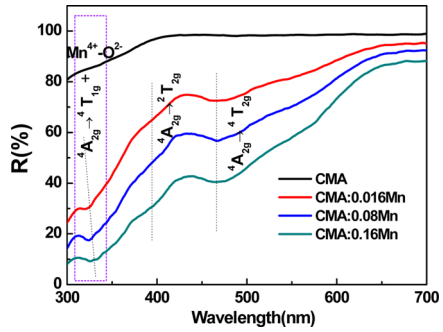

Figure 3. Representative diffuse reflection spectra of CMA:$x$$Mn^{4+}$ (x = 0, 0.016, 0.08, 0.16).

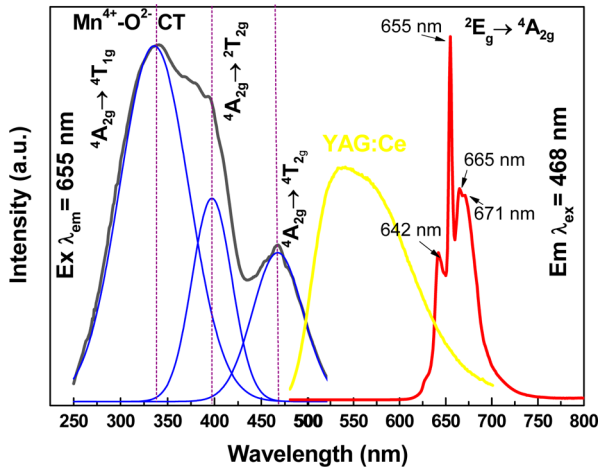

Figure 4. Room temperature PLE (λ_{em} = 655 nm) and PL (λ_{ex} = 468 nm) spectra of the CMA:0.08Mn^{4+} sample. The solid blue line represent data fit using Gaussian function. The vertical dashed lines are a guide for the eye. The yellow line represents the referenced emission spectrum of commercial YAG:Ce^{3+} phosphor under 468 nm light excitation.

can be fitted by three Gaussian curves, corresponding well with the DR spectrum. It is worth noting that the spectral overlap between the excitation of CMA:Mn^{4+} and the emission of commercial YAG:Ce^{3+} is rather small, thus the risk of photon reabsorption, often occurring between nitride red phosphor and YAG:Ce^{3+} yellow phosphor, can be greatly reduced. On the other hand, the phosphor shows intense red emission in the wavelength range between 600 and 750 nm with a maximum located at 655 nm (15 267 cm^{-1}) upon blue-light excitation. This red-emitting band consists of four distinguishable Stokes/anti-Stokes sidebands at 642, 655, 665 and 671 nm respectively, arising from the different vibrational modes of ^2E_g, $^2T_{2g} \rightarrow {}^4A_{2g}$ transitions for the $3d^3$ electrons in the $[MnO_6]^{8-}$ octahedral complex.[35] Because of the spin- and parity-forbidden nature of these transitions, the zero-phonon band is very weak and therefore unable to be identified. The calculated coordinate value (x, y) of the International Commission on Illumination (CIE) is (0.7205, 0.2778), similar to that of the commercial $3.5MgO{\cdot}3.5MgF_2{\cdot}GeO_2$:$Mn^{4+}$ (MMG:Mn^{4+}) red phosphors,[36,37] indicating its potential to enhance the color rendering performance of w-LED.

A series of PL spectra curves for CMA:0.08Mn^{4+} sample as a function of temperature from 77 to 300 K are shown in Figure 5a. Note that the integrated emission intensity of the PL spectrum increases at first with increasing temperature and then

dx.doi.org/10.1021/am507316b | ACS Appl. Mater. Interfaces 2014, 6, 22905−22913

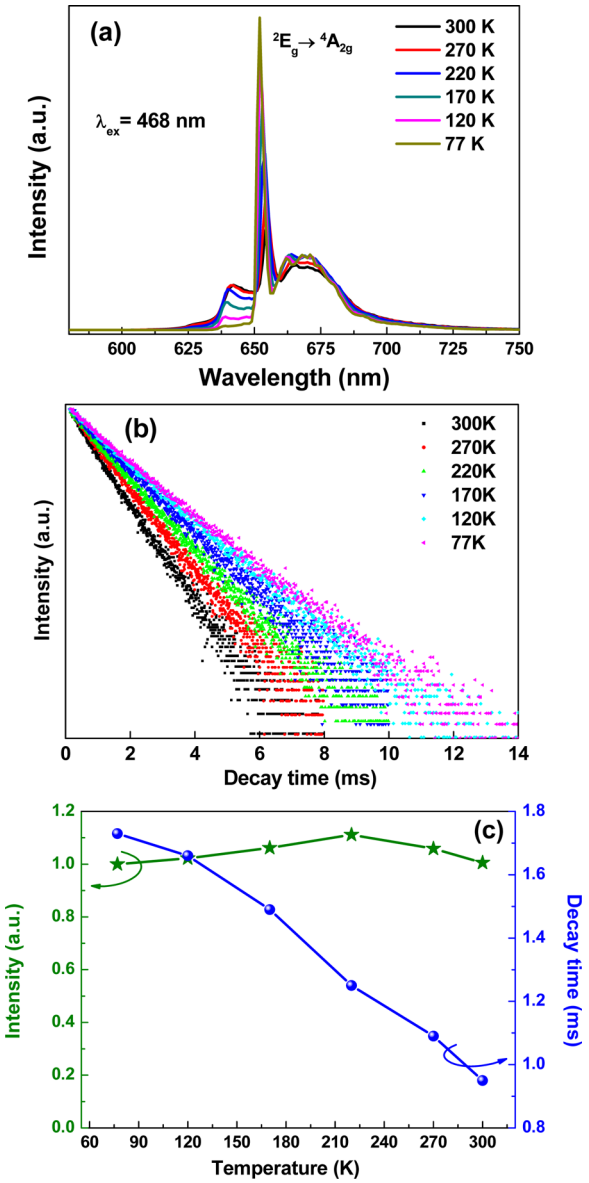

Figure 5. (a) Temperature-dependent emission spectra and (b) decay curves of CMA:0.08Mn^{4+} under excitation at 468 nm; (c) dependence of the average decay lifetime and the integrated emission intensity on temperature in CMA:0.08Mn^{4+}.

decreases when temperature is beyond 220 K, as illustrated in Figure 5c. The initial elevation is believed causing by the thermal population of higher vibrational states and thus the increase of the anti-Stokes sideband (e.g., 642 nm emission band), which compensates and overtakes the intrinsic thermal quenching effect.[38] With further increasing the temperature, the influence of nonradiative transition at elevated temperature becomes most dominant, resulting in the weakening of emission intensity. It is also found that a gradual peak red shift occurs with increasing temperature (see Figure S1, Supporting Information). This phenomenon can be explained by the Varshini equation of $E(T) = E_0 - aT^2/T + b$,[39,40] where $E(T)$ is the energy difference between excited states and ground states at a temperature T, E_0 is the energy difference at 0 K, a and b are fitting parameters. The fluorescence decay curves of the Mn^{4+}: ^2E_g, $^2T_{2g} \rightarrow {}^4A_{2g}$ also reveal a strong dependence on the temperature, as presented in Figure 5b,c. As the temperature increases, the calculated lifetime is gradually decreased from 1.73 to 0.89 ms because the nonradiative transition probability at a low temperature is lower than that at a high temperature.

Tanabe–Sugano energy-level diagram (Figure 6) illustrates the dependence of energy levels of Mn^{4+} on the octahedral

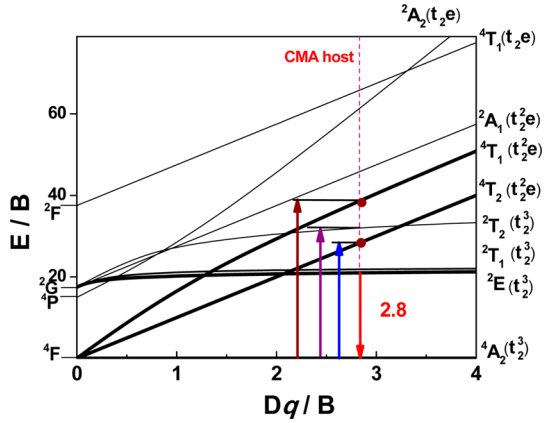

Figure 6. Tanabe–Sugano energy-level diagram for Mn^{4+} in the octahedral site of CMA host, wherein the ground electronic state ($^4A_{2g}$) and the lowest excited state (^2E_g) come from the t^3_2 configuration, whereas the $^4T_1$ and $^4T_2$ levels arise from the t^2_2e electronic orbital.

crystalline field of CMA crystal, in which the values of crystal-field strength (Dq) can be determined by the mean peak energy (21 367 cm^{-1}) of the $^4A_{2g} \rightarrow {}^4T_{2g}$ transition:[41]

$$\mathrm{Dq} = E(^4T_{2g} - {}^4A_{2g})/10 \quad (2)$$

On the basis of the peak energy difference (7618 cm^{-1}) between the $^4A_{2g} \rightarrow {}^4T_{2g}$ and $^4A_{2g} \rightarrow {}^4T_{1g}$ transitions, the Racah parameter B can be evaluated from the expression[42]

$$\frac{\mathrm{Dq}}{B} = \frac{15(x-8)}{(x^2-10x)} \quad (3)$$

where the parameter x is defined as

$$x = \frac{E(^4A_{2g} \rightarrow {}^4T_{1g}) - E(^4A_{2g} \rightarrow {}^4T_{2g})}{\mathrm{Dq}} \quad (4)$$

According to the peak energy of $^2E_g \rightarrow {}^4A_{2g}$ (15267 cm^{-1}) derived from the emission spectrum, the Racah parameter C can be calculated by the following expression:[22]

$$E(^2E_g - {}^4A_{2g})/B = 3.05C/B + 7.9 - 1.8B/\mathrm{Dq} \quad (5)$$

The values of Dq, B and C in the CMA:Mn^{4+} are then determined to be 2136, 754 and 3625 cm^{-1}, respectively, which are similar to those reported in the Mn^{4+}:$CaAl_{12}O_{19}$.[43] As previously stated, the crystal structure of the CMA is composed of the stacking sequence $(MS)_n$ structure. Therefore, this result indicates Mn^{4+} probably occupies the Al^{3+} sites in the M ($CaAl_{12}O_{19}$) layer other than the S ($Mg_2Al_4O_8$) layer of CMA. The nephelauxetic ratio β ($\beta = \beta_{complex} / B_{free\_ion}$, B_{free_ion} = 1160 cm^{-1}),[44] reflecting the effect of reducing electron–electron repulsion via ligands, is calculated to be 0.65. This value is similar to those reported in oxides, but higher than those in fluorides, due to the more ionic Mn^{4+}–F^- bonding than Mn^{4+}–O^{2-} bonding.[18]

dx.doi.org/10.1021/am507316b | ACS Appl. Mater. Interfaces 2014, 6, 22905–22913

The PLE and PL spectra of CMA:xMn^{4+} (x = 0.016, 0.032, 0.08, 0.16, 0.24 and 0.48) are shown in Figure 7a–c. Evidently, for all the samples, most of the spectral features are identical, except for the excitation band at around 340 nm, which shows obvious peak-shifting toward the long-wavelength side with increase of Mn^{4+} doping content (Figure S2, Supporting Information). This band can not be simply assigned to the Mn^{4+}: $^4A_{2g} \rightarrow {}^4T_{1g}$ transition, but is strongly possible due to the overlap between the Mn^{4+}: $^4A_{2g} \rightarrow {}^4T_{1g}$ and the Mn^{4+}–O^{2-} CT bands. It is postulated that the lattice expansion and/or the charge imbalance caused by gradual substitution of Mn^{4+} for Al^{3+} might be responsible for the red-shifting of the Mn^{4+}–O^{2-} CT band, which is similar to the case of Mo^{6+}–O^{2-} CT band in Eu^{3+}:NaLa$_4$(Mo$_3$O$_{15}$)F.[45] With an increase of Mn^{4+} content from 0.016 to 0.48, the PL intensity of Mn^{4+} increases at first, until it reaches a maximum at 0.08, then it decreases gradually, which is ascribed to concentration quenching.

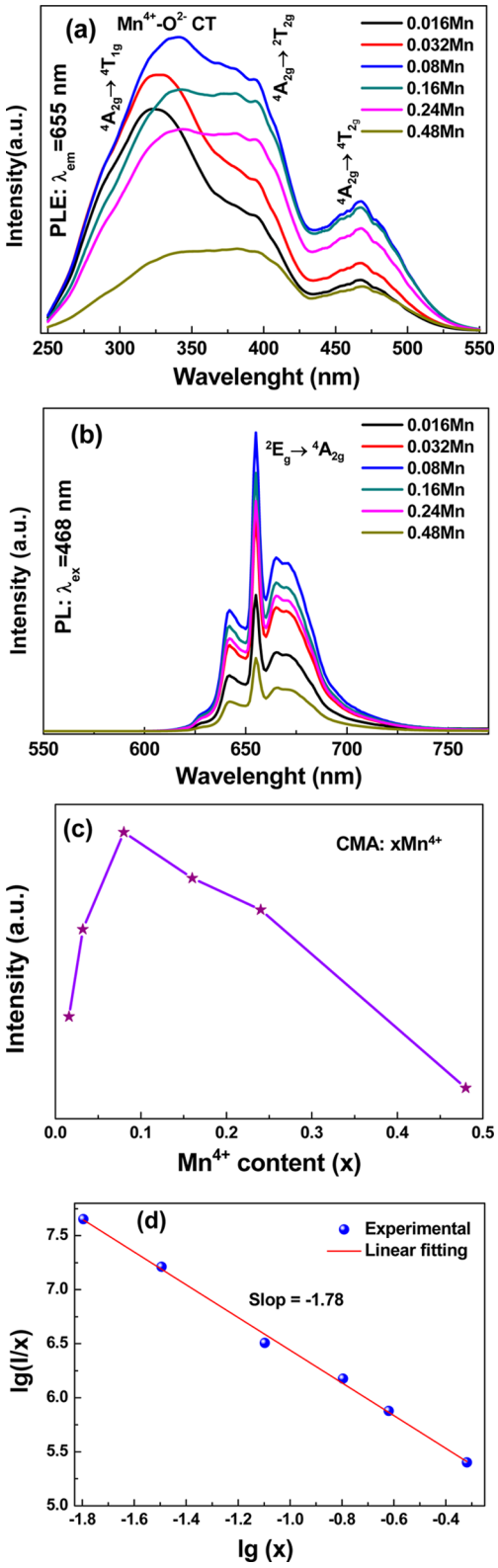

Figure 7. (a) PLE (λ_{em} = 665 nm) and (b) PL (λ_{ex} = 468 nm) spectra of the CMA:xMn^{4+} samples (x = 0.016, 0.032, 0.08, 0.16, 0.24 and 0.48, respectively); (c) PL intensity of Mn^{4+} as a function of Mn^{4+} doping concentration in the sample under excitation at 468 nm; (d) dependence of log(I/x) on log(x) according to eq 7.

As for the concentration quenching phenomenon, it is due to the occurrence of energy transfer within the nearest Mn^{4+} ions that is finally ended by a killer center. The involved energy transfer mechanism is not radiation reabsorption because there is no overlap between the PL and PLE spectra of Mn^{4+}. It might be related to exchange interaction or multipole–multipole interaction. To clarify this point, the critical transfer distance (R_c) needs to be calculated. Blasse[46] pointed out that if the activator is introduced solely on one site, there is, on average, one activator ion per V/x_cN (V is the volume of the unit cell, x_c the critical concentration, N the number of available sites for the dopant in the unit cell). Upon that, R_c is evaluated to be approximately twice the radius of a sphere with this volume:

$$R_c \approx 2\left(\frac{3V}{4\pi x_c N}\right)^{1/3} \quad (6)$$

In this case, V = 851.66 Å^3, obtained from Rietveld result, N = 32 and x_c = 0.08 and the critical transfer distance of Mn^{4+} in CMA is then calculated to be ~8.6 Å. Because the exchange interaction is dominant only for short critical transfer distance (typically, R_c < 5 Å), it is inferred that the concentration quenching mainly takes place via electric multipolar interaction between Mn^{4+} ions based on the Dexter theory.[47] The type of interaction between Mn^{4+} ions can be reflected by the following equation:[48]

$$I/x = K[1 + \beta(x)^{\theta/3}]^{-1} \quad (7)$$

where x is the activator concentration, K and β are the constants for each type of interaction in a given host lattice, θ is an indication of the electric multipolar character with θ = 6, 8, 10 corresponding to dipole–dipole (d-d), dipole–quadrupole (d-q) and quadrupole–quadrupole (q-q) interactions, respectively. In Figure 7d, the experimental results of the relationship between integrated emission intensity (I) and Mn^{4+} concentration (x) are fit well by using eq 7. The dependence of log(I/x) on log(x) appears to be linear with a slope $-(\theta/3) \approx -2$; therefore, the value θ is calculated as approximately 6, which indicates that the quenching mechanism is a d-d interaction for the Mn^{4+} center. The fluorescence decay curves of CMA:xMn^{4+} phosphors monitored at 655 nm with the excitation of 468 nm were measured at room temperature, as displayed in Figure 8. The decay process can be characterized by an average lifetime τ_{avg}, which is calculated by using eq 8:

$$\tau_{avg} = \int_0^\infty tI(t)\mathrm{d}t \Big/ \int_0^\infty I(t)\mathrm{d}t \quad (8)$$

dx.doi.org/10.1021/am507316b | ACS Appl. Mater. Interfaces 2014, 6, 22905–22913

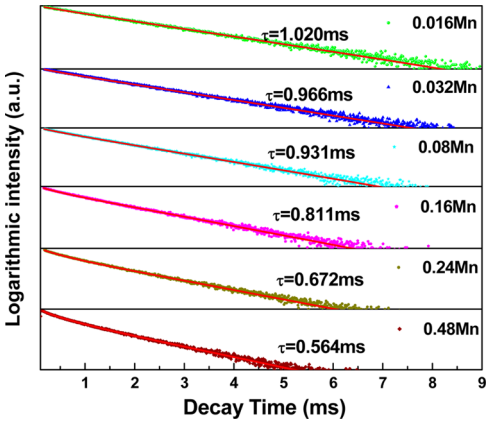

Figure 8. Decay curves of Mn^{4+}: ^2E_g, $^2T_{2g} \rightarrow {}^4A_{2g}$ in CMA:$x$$Mn^{4+}$ (x = 0.016, 0.032, 0.08, 0.16, 0.24 and 0.48, respectively) red phosphors when excited at 468 nm and monitored at 655 nm.

where $I(t)$ is the luminescence intensity of the CMA:$x$$Mn^{4+}$ sample at time t. The estimated lifetimes of Mn^{4+} are in a microsecond range, which is indicative of the forbidden character of the intra-d-shell transitions in Mn^{4+} ions. As expected, with the increment of Mn^{4+} content, the decay curves gradually deviate from a monoexponential decay mode and the τ_{avg} monotonously decreases from 1.020 to 0.564 ms, ascribed to the nonradiative energy migration among the Mn^{4+} ions.

3.3. Performance of LED Devices Based on the PiG Containing CMA:Mn^{4+} and YAG:Ce^{3+} Phosphors. To validate the availability of as-synthesized CMA:Mn^{4+} red phosphor for high-powered w-LED application, we introduced it into the YAG:Ce^{3+} PiG color converter innovatively developed in our lab,[30] aiming to solve the problem of red deficiency of the product.

First, the PiG containing merely CMA:0.08Mn^{4+} phosphor ("1-phosphor" sample) was prepared and characterized by using XRD, SEM and spectroscopic measurements to reveal the influence of glass-melting procedure on the microstructure and luminescent performance of CMA:Mn^{4+} phosphors. As shown in Figure 9a, the XRD pattern of CMA PiG exhibits identical diffraction peaks as those of CMA powder, indicating successful incorporation of CMA:Mn^{4+} into the glass host. The amorphous hump is originated from the glass matrix. The SEM image of a casually selected PiG piece shown in Figure 9c

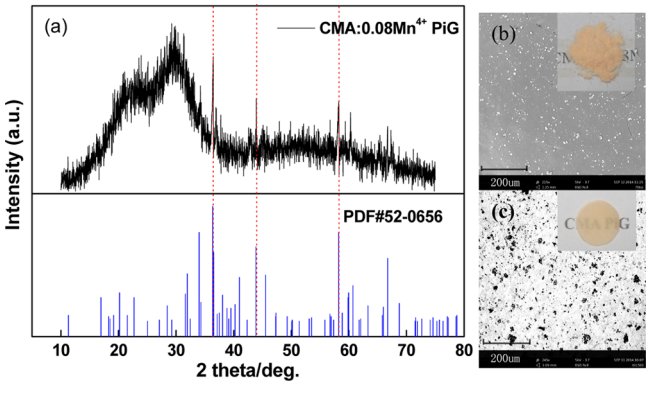

Figure 9. (a) XRD pattern of CMA:0.08Mn^{4+} PiG; (b) and (c) SEM images of the CMA:0.08Mn^{4+} powder and the PiG sample embedding 9 wt % CMA:0.08Mn^{4+}; insets in panels b and c show photographs of the corresponding samples.

reveals that the mean size of CMA particles is ~20 μm, in well accordance with that of the presynthesized CMA:Mn^{4+} powders exhibited in Figure 9b, suggesting the corrosion of CMA:Mn^{4+} particles by the glass melt at 570 °C is negligible. It is also found that the CMA:Mn^{4+} particles are distributed quite homogeneously in the glass matrix. The insets of Figure 9b,c present the digital photographs of the CMA:0.08Mn^{4+} powder and the corresponding PiG sample embedding 5 wt % CMA:0.08Mn^{4+}. Because of the refractive index difference between the mother glass and the CMA crystals, the PiG appears to be semitransparent. As expected, the steady-state PL spectrum (Figure 10a) and luminescent kinetic analysis (Figure

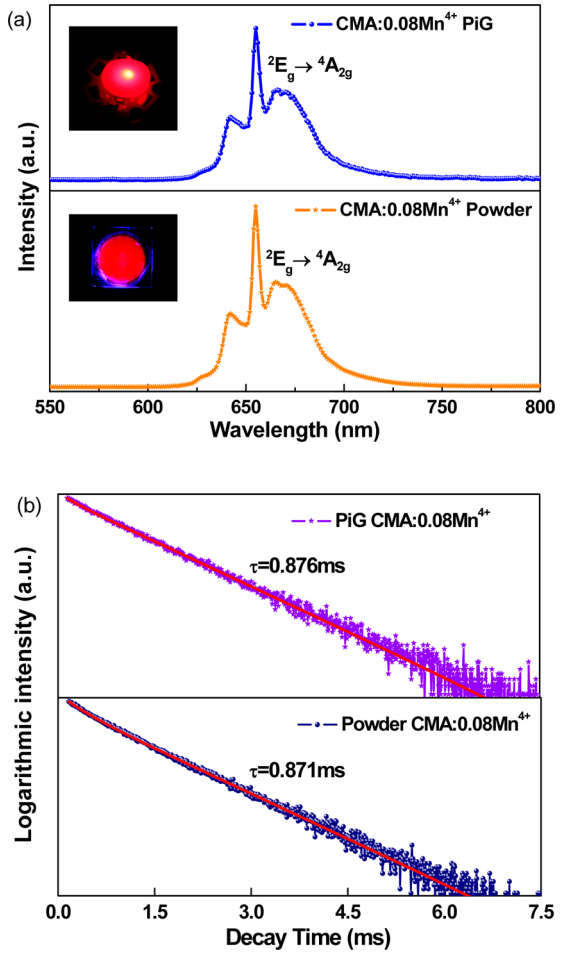

Figure 10. (a) PL spectra and (b) decay curves of the CMA:0.08Mn^{4+} powder and the corresponding PiG sample; insets in panel a show photographs of the corresponding samples under blue-light excitation.

10b) of CMA:Mn^{4+} PiG keep almost unchanged in comparison with those of CMA:Mn^{4+} powder. Both of the CMA:Mn^{4+} powder and the PiG present a sound eye-visible red-emitting light upon driven by a blue chip (see the luminescent photographs in the insets of Figure 10a). All these results demonstrate the successful incorporation of CMA:Mn^{4+} crystals into the glass host. The luminescence quantum efficiencies of CMA:0.08Mn^{4+} PiG and CMA:0.08Mn^{4+} powder were measured respectively, as demonstrated in Figure S3 (Supporting Information). The internal and external quantum efficiencies for CMA:Mn^{4+} powder are 35.6% and 16.0%, whereas those for CMA:Mn^{4+} PiG are 33.8% and 15.4%.

dx.doi.org/10.1021/am507316b | ACS Appl. Mater. Interfaces 2014, 6, 22905−22913

Evidently, the encapsulation of CMA:Mn^{4+} powder in glass influences the quantum efficiency insignificantly.

Then, we fabricated a "2-phosphor" PiG color converter by incorporating y wt % homemade CMA:0.08Mn^{4+} (y = 0, 1, 3, 5, 7, 9) and 5 wt % commercial YAG:Ce^{3+} phosphors together into the glass matrix. The typical internal quantum efficiency of PiG sample embedded with 5 wt % CMA:0.08Mn^{4+} and 5 wt % YAG:Ce^{3+} was measured to be 76.8%, as shown in Figure S4 (Supporting Information). The electroluminescent (EL) spectra of such PiGs with varied weighted contents of CMA:Mn^{4+}, driven under 350 mA current, are shown in Figure 11. The measured photometric and chromaticity

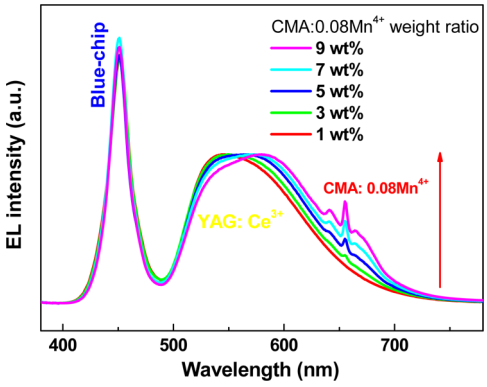

Figure 11. EL spectra of w-LED devices fabricated by coupling InGaN blue chip with PiG color converters containing 5 wt % YAG:Ce^{3+} and y wt % CMA:0.08Mn^{4+} (y = 1, 3, 5, 7, 9) phosphors. The driven current is 350 mA.

Table 1. Measured Photometric and Chromaticity Parameters for the PiG-based w-LEDs

		CIE coordinates				
no.	CMA:Mn^{4+} content (wt %)	x	y	CCT (K)	R_a	luminous efficiency (lm/W)
a	0	0.312	0.333	6674	70.0	124.6
b	1	0.332	0.347	6235	71.7	115.3
c	3	0.347	0.360	5511	74.2	94.7
d	5	0.362	0.374	5057	77.8	80.8
e	7	0.378	0.394	4512	81.3	72.2
f	9	0.395	0.416	3896	85.5	58.3

parameters are listed in Table 1. Obviously, with increase of CMA:Mn^{4+} contents from 0 wt % to 9 wt %, the PL spectra show an almost linear increase in Mn^{4+} red emissive component. Accordingly, appearance of the emitted white-light evolves gradually from cool to warm (Figure 12), the CIE coordinate changes from point a (0.312, 0.333) to point f (0.395, 0.416), the CCT decreases monotonously from 6674 to 3896 K and the CRI increases from 70.0 to 85.5. These results demonstrate that the introduction of CMA:Mn^{4+} red phosphors into the YAG:Ce^{3+} PiG gives rise to more suitable CCT and CRI values in the high-powered w-LED for indoor applications. Unfortunately, the luminous efficiency of the samples declines from 124.6 to 58.3 lm/W, probably caused by the reduced light extraction for more opaque of the PiG when more CMA:Mn^{4+} is added. However, the value of 70−80 lm/W

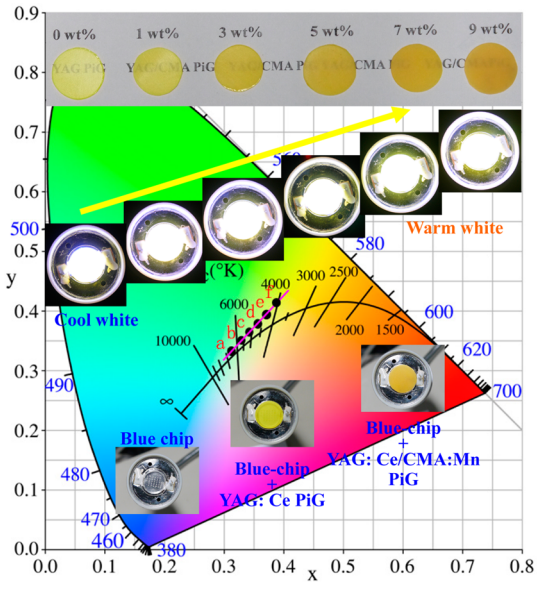

Figure 12. CIE chromaticity diagram of w-LEDs fabricated by coupling 5 wt % YAG:Ce^{3+} and y (y = 0, 1, 3, 5, 7, 9) wt % CMA:Mn^{4+} embedded PiG with blue chips; insets show photographs of the PiG samples with varied CMA:Mn^{4+} weighted contents, the corresponding LED packages and their electroluminescence driven by a 350 mA current.

in the samples containing 5% or 7% CMA:Mn^{4+} is still acceptable for general lighting.

4. CONCLUSION

In summary, a novel Mn^{4+}-activated $CaMg_2Al_{16}O_{27}$ red-emitting phosphor of high purity has been successfully synthesized by a high-temperature solid-state sintering method. The excitation and reflectance spectra show broad absorption of Mn^{4+}: $^4A_{2g} \rightarrow {}^4T_{2g}$ transition in the 420−500 nm region, which matches well with the emission of the commercial blue chip. Under excitation at 468 nm, the phosphors exhibit an intense red emission band peaked at 655 nm and the corresponding CIE coordinate is (0.7205, 0.2778). The optimized Mn^{4+} doping concentration is determined to be 0.08 mol, beyond which the d-d interaction-based energy transfer between Mn^{4+} centers would result in the concentration quenching. According to the Tanabe−Sugano diagram, the Racah parameters B and C and the crystal-field parameter 10Dq are calculated. In contrast to the case in Mn^{4+}-activated fluorides, the nephelauxetic effect in CMA is found strongly affecting the luminescence of Mn^{4+}. To evaluate the suitability of CMA:Mn^{4+} as red converters, they were introduced into the YAG:Ce^{3+} PiG and then coupled with the blue-chips, aiming to achieve warm white light. The XRD, SEM and spectroscopic measurements demonstrate successful incorporation of CMA crystals into the glass host without influencing their luminescent property remarkably. Driven by a 350 mA current, the assembled high-powered w-LED device shows a tunable R_a between 70 and 85.5 and CCT between 6674 and 3896 K by simply changing the red-phosphor weight ratio. It is proposed that the developed CMA:Mn^{4+} phosphors and the related PiGs would have desirable potential for applications in the high-powered warm w-LEDs.

■ ASSOCIATED CONTENT

Supporting Information

Temperature dependent PL emission spectra of CMA:0.08Mn^{4+} phosphor (Figure S1). The normalized PLE spectra of CMA:$x$$Mn^{4+}$ samples (x = 0.016, 0.032, 0.08, 0.16, 0.24, 0.48) in the region of 250 to 400 nm. (Figure S2). The excitation line and emission spectra of (a) CMA:0.08Mn^{4+} powders and (b) CMA:0.08Mn^{4+} PiG (Figure S3). The excitation line and emission spectrum of PiG sample embedded with 5 wt % YAG:Ce^{3+} and 5 wt % CMA:0.08Mn^{4+} microcrystals measured using an integrating sphere (Figure S4). This material is available free of charge via the Internet at http://pubs.acs.org.

■ AUTHOR INFORMATION

Corresponding Authors

*H. Lin. E-mail: lingh@fjirsm.ac.cn. Tel/Fax: +86-591-83751401.

*Y. Wang. E-mail: yswang@fjirsm.ac.cn. Tel/Fax: +86-591-83705402.

Notes

The authors declare no competing financial interest.

■ ACKNOWLEDGMENTS

This work was supported by National Natural Science Foundation of China (11204301, 51472242, 51172231, 21271170, 11304312), the key innovation project of Haixi Institute of CAS (SZD13001) and Key Laboratory of Design and Assembly of Functional Nanostructures, Chinese Academy of Science (2013DP173231).

■ REFERENCES

(1) Schubert, E. F.; Kim, J. K. Solid-State Light Sources Getting Smart. *Science* **2005**, *308*, 1274−1278.

(2) Höppe, H. A. Recent Developments in the Field of Inorganic Phosphors. *Angew. Chem., Int. Ed.* **2009**, *48*, 3572−3582.

(3) Wang, D. Y.; Huang, C. H.; Wu, Y. C.; Chen, T. M. $BaZrSi_3O_9$:Eu^{2+}: A Cyan-Emitting Phosphor with High Quantum Efficiency for White Light-Emitting Diodes. *J. Mater. Chem.* **2011**, *21*, 10818−10822.

(4) Liu, W. R.; Huang, C. H.; Yeh, C. W.; Tsai, J. C.; Chiu, Y. C.; Yeh, Y. T.; Liu, R. S. A Study on the Luminescence and Energy Transfer of Single-Phase and Color-Tunable $KCaY(PO_4)_2$:Eu^{2+}, Mn^{2+} Phosphor for Application in White-Light LEDs. *Inorg. Chem.* **2012**, *51*, 9636−9641.

(5) Ravichandran, D.; Roy, R.; White, W. B.; Erdei, S. Synthesis and Characterization of Sol-Gel Derived Hexa-Aluminate Phosphors. *J. Mater. Res.* **1997**, *12*, 819−824.

(6) Pawade, V. B.; Dhoble, S. J. Novel Blue-Emitting $SrMg_2Al_{16}O_{27}$:Eu^{2+} Phosphor for Solid-State Lighting. *Luminescence* **2011**, *26*, 722−727.

(7) Denault, K. A.; Gerorge, N. C.; Paden, S. R.; Brinkley, S.; Mikhailovsky, A. A.; Neuefeind, J.; DenBaars, S. P.; Seshardri, R. A Green-Yellow Emitting Oxyfluoride Solid Solution Phosphor $Sr_2Ba(AlO_4F)_{1-x}(SiO5)_x$:$Ce^{3+}$ for Thermally Stable, High Color Rendition Solid State White Lighting. *J. Mater. Chem.* **2012**, *22*, 18204−18213.

(8) Han, J. Y.; Im, W. B.; Lee, G. Y.; Jeon, D. Y. Near UV-Pumped Yellow-Emitting Eu^{2+}-Doped $Na_3K(Si_{1-x}Al_x)_8O_{16\pm\delta}$ Phosphor for White-Emitting LEDs. *J. Mater. Chem.* **2012**, *22*, 8739−8798.

(9) Li, J. J.; Chen, J. D.; Wei, R. F.; Guo, H. Combined White Luminescence from Eu^{3+}, ML-Ag Particles and Ag^+ in Ag-Eu^{3+} Co-Doped H_3BO_3-BaF_2 Glasses. *J. Am. Ceram. Soc.* **2012**, *95*, 1208−1211.

(10) Yang, L.; Chen, M. X.; Lv, Z. C.; Wang, S. M.; Liu, X. G.; Liu, S. Preparation of A YAG:Ce Phosphor Glass by Screen-Printing Technology and Its Application in LED Packaging. *Opt. Lett.* **2013**, *38*, 2240−2243.

(11) Li, Y. Q.; van Steen, J. E. J.; van Krevel, J. W. H.; Botty, G.; Delsing, A. C. A.; DiSalvo, F. J.; de With, G.; Hintzen, H. T. Luminescence Properties of Red-Emitting $M_2Si_5N_8$:Eu^{2+} (M = Ca, Sr, Ba) LED Conversion Phosphors. *J. Alloys Compd.* **2006**, *417*, 273−279.

(12) Uheda, K.; Hirosaki, N.; Yamamoto, Y.; Naito, A.; Nakajima, T.; Yamamoto, H. Luminescence Properties of a Red Phosphor, $CaAlSiN_3$:Eu^{2+}, for White Light-Emitting Diodes. *Electrochem. Solid-State Lett.* **2006**, *9*, H22−H25.

(13) Smet, P. F.; Parmentier, A. B.; Poelman, D. Selecting Conversion Phosphors for White Light-Emitting Diodes. *J. Electrochem. Soc.* **2011**, *158*, R37−R54.

(14) Zhu, H. M.; Lin, C. C.; Luo, W. Q.; Shu, S. T.; Liu, Z. G.; Liu, Y. S.; Kong, J. T.; Ma, E.; Cao, Y. G.; Liu, R. S.; Chen, X. Y. Highly Efficient Non-Rare-Earth Red Emitting Phosphor for Warm White Light-Emitting Diodes. *Nat. Commun.* **2014**, *5*, 4312.

(15) Okamoto, S.; Yamamoto, H. Luminescent-Efficiency Improvement by Alkaline-Earth Fluorides Partially Replacing MgO in 3.5$MgO{\cdot}0.5MgF_2{\cdot}GeO_2$:$Mn^{4+}$ Deep-Red Phosphors for Light Emitting Diodes. *J. Electrochem. Soc.* **2010**, *157*, J59−J63.

(16) Peng, M. Y.; Yin, X. W.; Tanner, P. A.; Liang, C. Q.; Li, P. F.; Zhang, Q. Y.; Qiu, J. R. Orderly-Layered Tetravalent Manganese-Doped Strontium Aluminate $Sr_4Al_{14}O_{25}$:Mn^{4+}: An Efficient Red Phosphor for Warm White Light Emitting Diodes. *J. Am. Ceram. Soc.* **2013**, *96*, 2870−2876.

(17) Tanabe, Y.; Sugano, S. On the Absorption Spectra of Complex Ions. I. *J. Phys. Soc. Jpn.* **1954**, *9*, 753−766.

(18) Brik, M. G.; Srivastava, A. M. On the Optical Properties of the Mn^{4+} Ion in Solids. *J. Lumin.* **2013**, *133*, 69−72.

(19) Takahashi, T.; Adachi, S. Mn^{4+}-Activated Red Photoluminescence in K_2SiF_6 Phosphor. *J. Electrochem. Soc.* **2008**, *155*, E183−E188.

(20) Li, P. F.; Peng, M. Y.; Yin, X. W.; Ma, Z. J.; Doing, G. P.; Zhang, Q. Y.; Qiu, J. R. Temperature Dependent Red Luminescence from a Distorted Mn^{4+} Site in $CaAl_4O_7$:Mn^{4+}. *Opt. Express* **2013**, *21*, 18943−18948.

(21) Srivastava, A. M.; Brik, M. G. Crystal Field Studies of the Mn^{4+} Energy Levels in the Perovskite, $LaAlO_3$. *Opt. Mater.* **2013**, *35*, 1544−1548.

(22) Brik, M. G.; Srivastava, A. M. Electronic Energy Levels of the Mn^{4+} Ion in the Perovskite, $CaZrO_3$. *ECS J. Solid State Sci. Technol.* **2013**, *2*, R148−R152.

(23) Göbbles, M.; Woermann, E.; Jung, J. The Al-rich Part of the System CaO-Al_2O_3-MgO: Part I. Phase Relationships. *J. Solid State Chem.* **1995**, *120*, 358−363.

(24) Iyi, N.; Göbbels, M.; Matsui, Y. The Al-rich Part of the System CaO-Al_2O_3-MgO: Part II. Structure Refinement of Two New Magnetoplumbite-Related Phases. *J. Solid State Chem.* **1995**, *120*, 364−371.

(25) Sako, E. Y.; Braulio, M. A. L.; Zinngrebe, E.; van der Laan, S. R.; Pandolfelli, V. C. In-Depth Microstructural Evolution Analyses of Cement-Bonded Spinel Refractory Castables: Novel Insights Regarding Spinel and CA_6 Formation. *J. Am. Ceram. Soc.* **2012**, *95*, 1732−1740.

(26) Chen, D. A.; Chen, Y. Transparent Ce^{3+}:$Y_3Al_5O_{12}$ Glass Ceramic for Organic-Resin-Free White-Light-Emitting Diodes. *Ceram. Int.* **2014**, *40*, 15325−15329.

(27) Zhang, X. J.; Huang, L.; Pan, F. J.; Wu, M. M.; Wang, J.; Chen, Y.; Su, Q. Highly Thermally Stable Single-Component White-Emitting Silicate Glass for Organic-Resin-Free White-Light-Emitting Diodes. *ACS Appl. Mater. Interfaces* **2014**, *6*, 2709−2717.

(28) Fujita, S.; Sakamoto, A.; Tanabe, S. Luminescence Characteristics of YAG Glass-Ceramic Phosphor for White LED. *IEEE J. Sel. Top. Quantum Electron.* **2008**, *14*, 1387−1391.

(29) Nakanishi, T.; Tanabe, S. Novel Eu^{2+}-Activated Glass Ceramics Precipitated with Green and Red Phosphors for High-Power White LED. *IEEE J. Sel. Top. Quantum Electron.* **2009**, *15*, 1171−1176.

(30) Zhang, R.; Lin, H.; Yu, Y. L.; Chen, D. Q.; Xu, J.; Wang, Y. S. A New-Generation Color Converter for High-Power White LED: Transparent Ce^{3+}:YAG Phosphor-in-Glass. *Laser Photonics Rev.* **2014**, *8*, 158−164.
(31) Jiao, M. M.; Jia, Y. C.; Lu, W.; Lv, W. Z.; Zhao, Q.; Shao, B. Q.; You, H. P. Structure and Photoluminescence Properties of Novel Ca_2NaSiO_4F:Re (Re = Eu^{2+}, Ce^{3+}, Tb^{3+}) Phosphors with Energy Transfer for White Emitting LEDs. *J. Mater. Chem. C* **2014**, *2*, 4304−4311.
(32) Bergstei, A.; White, W. B. Manganese-Activated Luminescence in $SrAl_{12}O_{19}$ and $CaAl_{12}O_{19}$. *J. Electrochem. Soc.* **1971**, *118*, 1166−1171.
(33) Pan, X. Y.; Liu, G. K. Enhancement of Phosphor Efficiency via Composition Modification. *Opt. Lett.* **2008**, *33*, 1816−1818.
(34) Lv, L. F.; Jiang, X. Y.; Huang, S. M.; Chen, X.; Pan, Y. X. The Formation Mechanism, Improved Photoluminescence and LED Applications of Red Phosphor K_2SiF_6:Mn^{4+}. *J. Mater. Chem. C* **2014**, *2*, 3879−3884.
(35) Srivastava, A. M.; Beers, W. W. Luminescence of Mn^{4+} in the Distorted Perovskite Gd_2MgTiO_6. *J. Electrochem. Soc.* **1996**, *143*, L203−L205.
(36) Kemeny, G.; Haake, C. H. Activator Center in Magnesium Fluorogermannate Phosphors. *J. Chem. Phys.* **1960**, *33*, 783−789.
(37) Xu, Y. D.; Wang, D.; Wang, L.; Ding, N.; Shi, M.; Zhong, J. G.; Qi, S. Preparation and Luminescent Properties of a New Red Phosphor ($Sr_4Al_{14}O_{25}$:Mn^{4+}) for White LEDs. *J. Alloys Compd.* **2013**, *550*, 226−230.
(38) Shao, Q. Y.; Lin, H. Y.; Hu, J. L.; Dong, Y.; Jiang, J. Q. Temperature-Dependent photoluminescence Properties of Deep-Red Emitting Mn^{4+}-Activated Magnesium Fluorogermanate Phosphors. *J. Alloys Compd.* **2013**, *552*, 370−375.
(39) Varshni, Y. P. Temperature Dependence of Energy Gap in Semiconductions. *Phys.* **1967**, *34*, 149−154.
(40) Kim, J. S.; Park, Y. H.; Kim, S. M.; Choi, J. C.; Park, H. L. Temperature-Dependent Emission Spectra of M_2SiO_4:Eu^{2+} (M = Ca, Ba) Phosphors for Green and Greenish White LEDs. *Solid State Commun.* **2005**, *133*, 445−448.
(41) Reisfeld, M. J.; Matwiyof, N. A.; Aspery, L. B. Asprey. Electronic Spectrum of Cesium Hexafluoromanganese (IV). *J. Mol. Spectrosc.* **1971**, *39*, 8−20.
(42) Henderson, B.; Imbusch, G. F. *Optical Spectroscopy of Inorganic Solids*; Clarendon Press: Oxford, U. K., 1989.
(43) Brik, M. G.; Pan, Y. X.; Liu, G. K. Spectroscopic and Crystal Field Analysis of Absorption and Photoluminescence Properties of Red Phosphor $CaAl_{12}O_{19}$:Mn^{4+} Modified by MgO. *J. Alloys Compd.* **2011**, *509*, 1452−1456.
(44) Uylings, P. H. M.; Raassen, A. J. J.; Wyart, J. F. Energies of N Equivalent Electrons Expressed in Terms of Two-Electron Energies and Independent Three-Electron Parameters: A New Complete Set of Orthogonal Operators. II. Application to $3d^N$ Configurations. *J. Phys. B: At. Mol. Phys.* **1984**, *17*, 4103−4126.
(45) Qi, S. Y.; Xie, H. D.; Huang, Y. L.; Kim, S. I.; Seo, H. A Narrow Red-Emitting Phosphor of $NaLa_4[Mo_3O_{15}]F$:Eu^{3+} with Broad Excitation Band Extending in Blue Wavelength Region. *J. Opt. Mater. Express* **2014**, *4*, 190−197.
(46) Blasse, G.; Dirksen, G. J. Luminescence and Crystal-Structure of $LiNbGeO_5$. *J. Solid State Chem.* **1986**, *65*, 283−286.
(47) Dexter, D. L. A Theory of Sensitized Luminescence in Solids. *J. Chem. Phys.* **1953**, *21*, 836−850.
(48) Xia, Z. G.; Zhang, Y. Y.; Molokeev, M. S.; Atuchin, V. V. Structural and Luminescence Properties of Yellow-Emitting NaScSi$_2O_6$:Eu^{2+} Phosphors: Eu^{2+} Site Preference Analysis and Generation of Red Emission by Codoping Mn^{2+} for White Light-Emitting Diode Application. *J. Phys. Chem. C* **2013**, *117*, 20847−20854.